

LETTERS

The depth distribution of azimuthal anisotropy in the continental upper mantle

Federica Marone¹† & Barbara Romanowicz¹

The most likely cause of seismic anisotropy in the Earth's upper mantle is the lattice preferred orientation of anisotropic minerals such as olivine^{1,2}. Its presence reflects dynamic processes related to formation of the lithosphere as well as to present-day tectonic motions. A powerful tool for detecting and characterizing upper-mantle anisotropy is the analysis of shear-wave splitting measurements. Because of the poor vertical resolution afforded by this type of data, however, it has remained controversial whether the splitting has a lithospheric origin that is 'frozen-in' at the time of formation of the craton³, or whether the anisotropy originates primarily in the asthenosphere, and is induced by shear owing to present-day absolute plate motions⁴. In addition, predictions from surface-wave-derived models are largely incompatible with shear-wave splitting observations^{5,6}. Here we show that this disagreement can be resolved by simultaneously inverting surface waveforms and shear-wave splitting data. We present evidence for the presence of two layers of anisotropy with different fast-axis orientations in the cratonic part of the North American upper mantle. At asthenospheric depths (200–400 km) the fast axis is sub-parallel to the absolute plate motion, confirming the presence of shear related to current tectonic processes, whereas in the lithosphere (80–200 km), the orientation is significantly more northerly. In the western, tectonically active, part of North America, the fast-axis direction is consistent with the absolute plate motion throughout the depth range considered, in agreement with a much thinner lithosphere.

Shear-wave (SKS) splitting data provide estimates of the apparent strength of anisotropy and the direction of the fast axis, representing the integrated effect of anisotropy over the whole upper mantle, assuming that the anisotropic tensor has a horizontal axis of symmetry and that anisotropy is weak⁷. Surface-wave data also have sensitivity to azimuthal anisotropy and provide complementary information. In particular, surface waves have much better depth resolution compared to SKS splitting measurements, although their lateral resolution is limited to long wavelengths. Yet, until now, SKS splitting measurements predicted by surface-wave-derived models of azimuthal anisotropy have not matched the observed SKS splitting directions in many continental regions^{5,6}. This puzzling discrepancy has been attributed to short-wavelength variations in anisotropy that are not resolvable with presently available surface-wave data⁸. Here we show that these two data sets can be largely reconciled when one realizes that surface-wave inversions generally have reduced sensitivity to azimuthal anisotropy below a depth of 250 km, and, in fact, underestimate the effect of deeper anisotropy with a different prevailing orientation.

We have developed a tomographic procedure to invert three-component long period fundamental and overtone surface waveforms for both radial and azimuthal anisotropy (see Methods Summary). The

radial anisotropic part of this study confirms earlier global-scale results⁹ and is presented elsewhere¹⁰. Here we discuss the results of inversion for lateral and depth variations in azimuthal anisotropy. The waveform data allow us to resolve lateral variations in strength and direction of the fast axis of anisotropy with a wavelength of about 1,000 km. Because we include overtones in our inversion, we are able to resolve variations of anisotropy down to depths in excess of 400 km (see Supplementary Figs 2–5).

The three-dimensional model obtained using our waveform data set alone (model A) presents several striking features (Fig. 1a, b, c). At 100 km depth, anisotropy is larger than 2% throughout most of the continent and defines two distinct domains with different orientations of the fast axis. In the young, active western part of the continent, characterized by a thin lithosphere, we find good agreement between the direction of the fast axis and that of absolute plate motion (APM)¹¹ (see also Supplementary Fig. 1). In the old, stable part of North America, to the east of the Rocky Mountains, azimuthal anisotropy shows lateral variations in strength and the fast-axis direction is not, on average, consistent with the APM direction. Deeper than 200 km, the character of anisotropy changes significantly beneath the stable part of North America, and the fast-axis direction becomes coherent throughout the continent, and sub-parallel to the APM direction (Fig. 1c, Supplementary Fig. 1).

We have also collected SKS splitting results for stations in North America from the literature (see Supplementary Table 1) and included these measurements as constraints in our inversion, using an established formalism that relates the apparent splitting time and fast-axis direction to the corresponding depth distribution of anisotropy⁵ (see Methods Summary). The model thus obtained (model B) shows a distribution of fast-axis orientations very similar to that in model A at shallow depth (Fig. 1d, e, f; Fig. 2). Moreover, the fit to the waveform data is as good as in model A, while the fit to the SKS splitting measurements is much improved (Fig. 3). The most striking difference is the strength of anisotropy inferred in the deeper domain (200–400 km), which is on average at least twice as large in model B (Fig. 1c, f). This observation indicates that the surface-wave data alone, even including overtones, rapidly lose sensitivity to the strength of azimuthal anisotropy at depths greater than ~200–250 km. This is confirmed by synthetic tests, which show that the direction of the fast axis is well resolved throughout the upper mantle, as is the strength of anisotropy at shallow depths (Fig. 4, Supplementary Figs 2–5), whereas at greater depth, amplitudes are significantly underestimated, in spite of the inclusion of overtones. Constraints from SKS splitting help to reduce this amplitude loss.

One striking feature of our models is the presence of two distinct depth domains of anisotropy, characterized by different fast-axis directions, under the stable part of the continent. Only the deeper domain shows a fast-axis direction compatible with the APM direction

¹Berkeley Seismological Laboratory, 209 McCone Hall, Berkeley, California 94720, USA. †Present address: Swiss Light Source, WLG/135, Paul Scherrer Institute, 5232 Villigen, Switzerland.

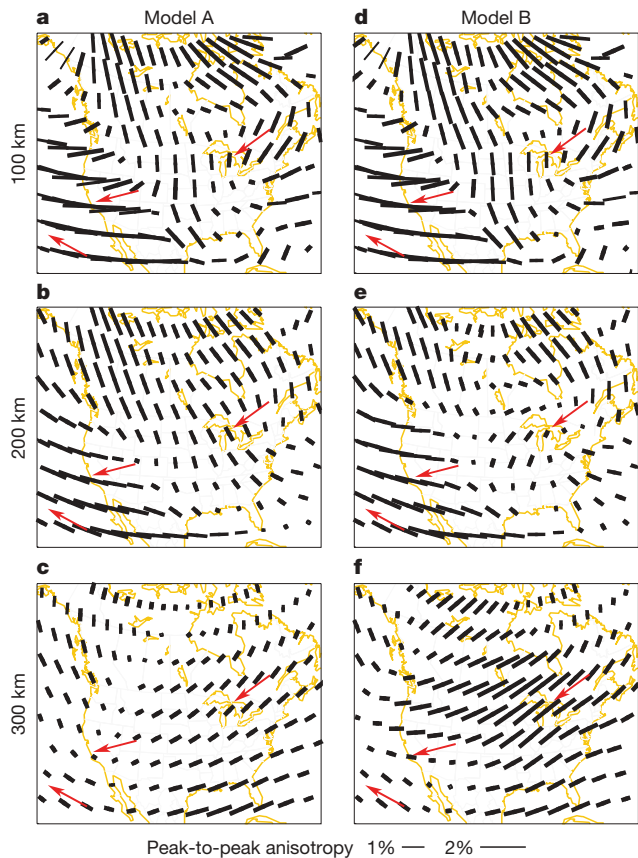


Figure 1 | Horizontal slices at three different depths showing azimuthal anisotropy in the North American upper mantle. Model A (a–c) was derived using uniquely fundamental mode and overtone surface waveforms. Model B (d–f) was obtained by joint inversion of surface waveforms and SKS splitting measurements. The length of the black bars is proportional to the maximum amplitude of azimuthal anisotropy, and their azimuth is parallel to the axis of fast propagation. Red arrows indicate the APM direction in a hotspot reference frame¹¹. We note the sharp transition in the fast-axis direction of anisotropy at 100 km depth across the Rocky Mountain Front and its agreement with APM at 300 km everywhere.

(Fig. 2). In contrast, under the tectonically active western USA, where the lithosphere is thin, the fast-axis direction is stable with depth and consistent with the APM direction throughout the uppermost mantle (Fig. 2), while its strength is largest at 100 km and decreases with depth. At 100 km depth, we note a gradual rotation of the fast axis from east to west (Fig. 1d, e), compatible with the difference in APM direction between the North American and Pacific plates.

Horizontal shear in the asthenosphere due to the motion of tectonic plates over the underlying mantle has been invoked to explain

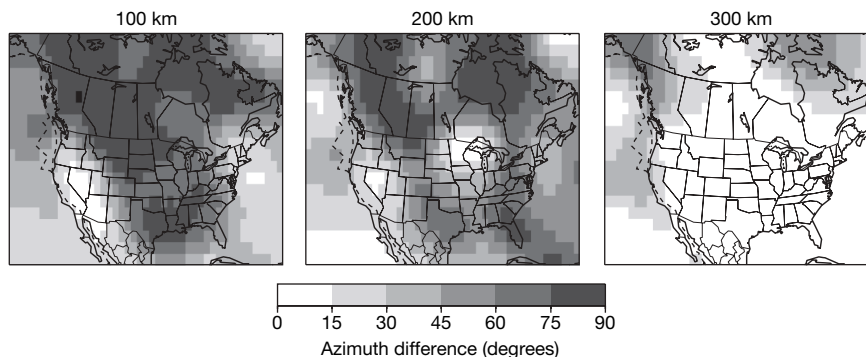


Figure 2 | Difference in azimuth between the axis of fast propagation in model B and the present-day APM direction. The APM is given in a hotspot

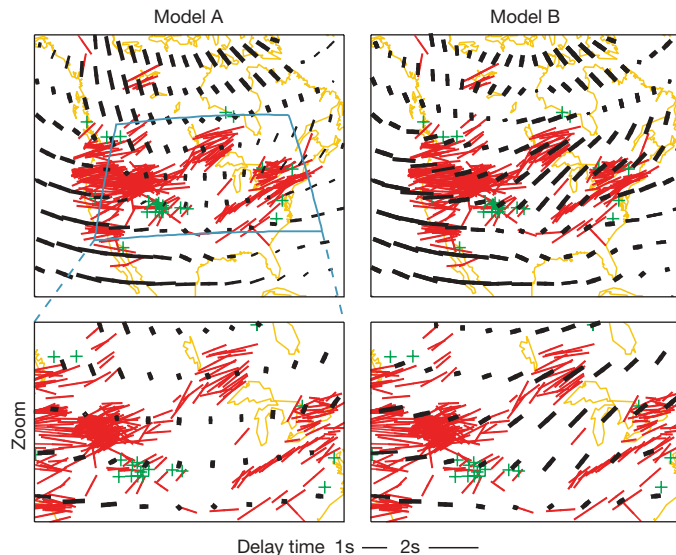


Figure 3 | Comparison of observed and predicted SKS splitting measurements. Observations (red) are from the literature (see Supplementary Table 1). Predictions (black) are from model A (left panel) and model B (right panel). Green crosses represent observed null measurements. The bottom panels show a magnification of the results for the region comprised by the blue boxed area. Variance reduction (see definition in Methods) is 0.71 in both models for surface waveforms and 0.11 in model A and 0.51 in model B for the SKS splitting data. Thus both models provide equal fits to surface waves but model B provides a significantly better fit to splitting data.

radial anisotropy at sub-lithospheric depths on the global scale⁹. The agreement between the APM direction and the fast-axis direction obtained in our models beneath the lithosphere–asthenosphere boundary, lends additional strength to this interpretation. Under oceanic basins, where the lithosphere is thin, surface-wave inversions based on shorter-period fundamental modes¹² also resolve the presence of two layers of anisotropy—lithospheric and asthenospheric—and strong azimuthal anisotropy aligned with APM is found at asthenospheric depths^{13,14}. Our results thus suggest that the deformation mechanism responsible for lattice preferred orientation in the asthenosphere is the same beneath continents and oceans, despite different lithospheric thicknesses. The average depth of the continental root¹⁰ under North America broadly agrees with the transition depth between the two imaged anisotropic layers (Fig. 1e) where anisotropy strength is minimum, so we infer that the lithosphere–asthenosphere boundary marks the limit between these two distinct anisotropic regimes, at varying depths under cratons, tectonically active North America and under oceans.

A recent global azimuthal anisotropic model⁶ derived from fundamental-mode and overtone surface waves showed weak anisotropy at

reference frame¹¹, and the same depths are shown as in Fig. 1.

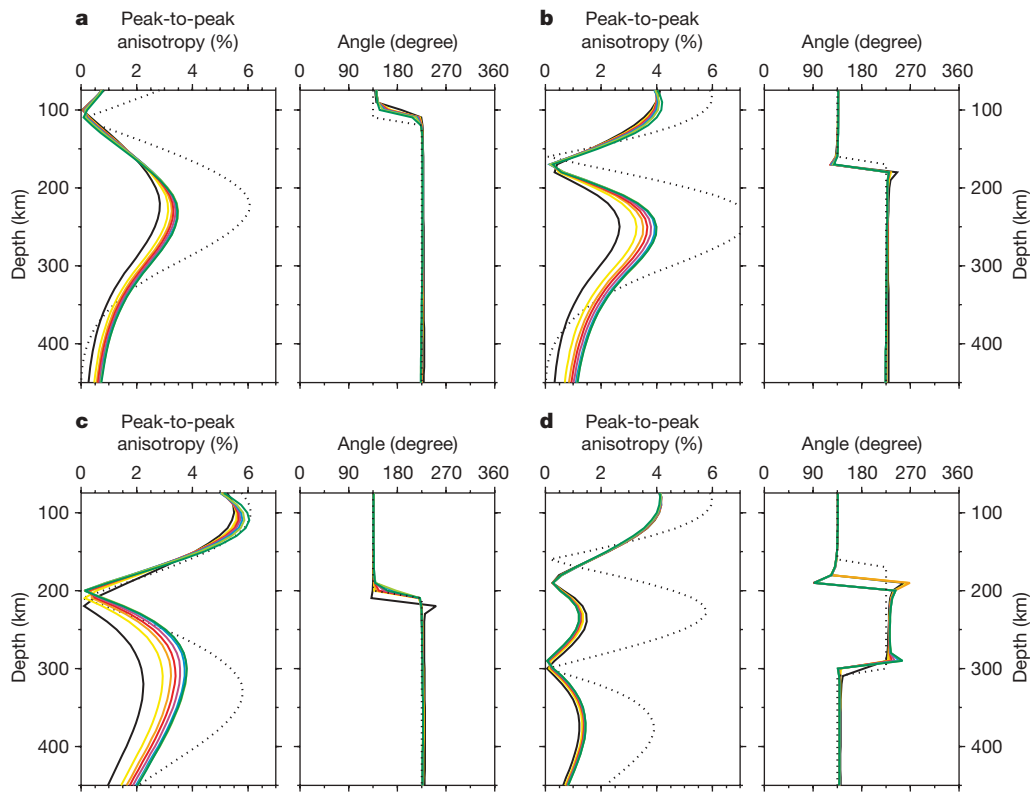


Figure 4 | Results of four resolution tests designed to assess the ability of our data set to resolve several anisotropic layers. In the synthetic input model, shown as a function of depth (dotted black line), azimuthal anisotropy is organized in two (a–c) or three (d) laterally homogeneous layers, with orthogonal fast-axis directions. Solid lines represent a variety of recovered models: results obtained using only the surface-wave data set

(black) or using surface waveforms and SKS splitting data together (other colours), with the weighting given to the SKS data increasing progressively from yellow to green. Model B was obtained with an intermediate weighting, corresponding to the red solid line. These one-dimensional vertical profiles have been extracted for a location in the central/eastern USA (latitude 45° N, longitude 95° W).

depths greater than 200 km under cratons, except under Australia, the fastest-moving continent. This result suggested a weak lithosphere–asthenosphere coupling beneath most continental regions, but was difficult to reconcile with the observed strong radial anisotropy at asthenospheric depths⁹. However, the present study shows that, under the North American continent, weak azimuthal anisotropy at asthenospheric depths is an artefact due to the reduced sensitivity of surface waves and that part of the signal can be recovered by including independent constraints. Thus, the North American lithospheric plate shows at least some degree of coupling with the underlying mantle.

The methodology used here to include SKS splitting constraints⁵ in the inversion also allows us to test how well our three-dimensional azimuthal anisotropic model predicts SKS splitting observations, a test which most existing models based on surface-wave data have failed. We find good agreement between observed and synthetic SKS splitting measurements for the tectonically active western US independently of the inclusion of additional body-wave constraints in the inversion (Fig. 3). As previously noted^{5,6}, compatibility between observed and predicted measurements is instead poor for the central and eastern USA (Fig. 3), when only surface waveforms are used to derive the model. In this case, the amplitude of the imaged anisotropy at depth is small (Fig. 1c) because it is underestimated (Fig. 4, Supplementary Figs 2–5) and therefore the predicted integrated anisotropic effect over depth on vertically travelling SKS waves is dominated by the shallow stronger signal, leading to the observed discrepancy. In contrast, the model we derived using the joint data set more accurately constrains the anisotropy strength below 200 km (Fig. 4, Supplementary Figs 2–5). While our model B, as expected, does not perfectly fit short-wavelength splitting variations such as are found in the Colorado plateau, it does a remarkably good job in the

eastern part of the continent (Fig. 3). Thus, our new anisotropic model, consistent with both surface- and body-wave data, at least at long wavelengths, offers a resolution to the long-standing debate on the depth, and hence the origin, of inferred azimuthal anisotropy from SKS splitting measurements in continental environments. We anticipate that a similar approach will help reconcile surface-wave and splitting results in other continents, in particular Australia^{6,15}.

The apparent splitting times and fast-axis directions of the SKS compilations used here do not directly provide information on the depth variation of anisotropy. That information is lost in the standard processing of raw SKS data, which averages out any azimuthal variations of the splitting parameters at each station. In addition, most studies so far do not have sufficient azimuthal coverage to resolve more than one layer of anisotropy, and generally find a fast-axis direction sub-parallel to the APM^{16–18} in the stable part of the continent. It is possible that the effect of the deeper anisotropic layer is dominant in these data because, in the lithosphere, the actual orientation of the fast axis may not be completely horizontal¹⁹, or may show complex variations. However, indications that two layers of anisotropy may be present have recently been emerging from shear-wave splitting data in central and eastern North America^{20–24}. Additional SKS splitting measurements from high-quality data from the Earthscope USArray deployment should shed additional light on this question.

METHODS SUMMARY

Our surface-waveform inversions are performed in the framework of normal-mode asymptotic coupling theory (NACT)²⁵, a normal-mode perturbation approach which takes into account coupling across branches, thus allowing us to represent the body-wave character of overtones. We compare observed and synthetic waveforms in the time domain. The effect of weak 3D isotropic and anisotropic heterogeneity is expressed through the local frequency shift for a

mode multiplet, and depends on the weighted integration over depth of 13 local anisotropic parameters, of which we only consider four: the isotropic S-velocity v_s , the anisotropic parameter ξ , and the azimuthal $2-\psi$ coefficients G_c and G_s (subscripts c and s indicate cosine and sine terms, respectively), where ψ is the local azimuth. Assuming weak anisotropy with a horizontal symmetry axis, station average SKS splitting parameters (apparent delay time δt and fast-axis direction Ψ) can be expressed simply in terms of the parameters G_c and G_s for periods longer than 10 s (ref. 5). For each single station with azimuthally averaged SKS splitting measurements, we add two equations, equally weighted, to the inverse problem, where the data are combinations of δt and Ψ into $\delta t \cos 2\Psi$ and $\delta t \sin 2\Psi$, which are linearly related to G_c and G_s . These quantities are also used to assess the goodness of fit of our models to observed splitting data (see Methods for further details). We can apply different weighting schemes for the contribution of surface waveforms and splitting data in the joint inversion. More details about our data coverage are provided in the Supplementary Information.

Full Methods and any associated references are available in the online version of the paper at www.nature.com/nature.

Received 3 November 2006; accepted 8 March 2007.

- Nicolas, A. & Christensen, N. I. in *Composition, Structure and Dynamics of the Lithosphere/Asthenosphere System* (eds Fuchs, K. & Froidevaux, C.) *Geodyn. Ser.* **16**, 111–123 (AGU, Washington DC, 1987).
- Babuška, V. & Cara, M. *Seismic Anisotropy in the Earth* (Kluwer Academic, Dordrecht, 1991).
- Silver, P. G. Seismic anisotropy beneath continents: probing the depth of geology. *Annu. Rev. Earth Planet. Sci.* **24**, 385–421 (1996).
- Vinnik, L. P., Makeyeva, L. I., Milev, A. Y. & Usenko, A. Y. Global patterns of azimuthal anisotropy and deformations in the continental mantle. *Geophys. J. Int.* **111**, 433–447 (1992).
- Montagner, J.-P., Griot-Pommer, D.-A. & Lavé, J. How to relate body wave and surface wave anisotropy? *J. Geophys. Res.* **105**, 19015–19027 (2000).
- Debayle, E., Kennett, B. L. N. & Priestley, K. Global azimuthal seismic anisotropy and the unique plate-motion deformation of Australia. *Science* **433**, 509–512 (2005).
- Vinnik, L. P., Kosarev, G. L. & Makeyeva, L. I. Anisotropy of the lithosphere from the observations of SKS and SKKS. *Proc. Acad. Sci. USSR [in Russian]* **278**, 1335–1339 (1984).
- Montagner, J.-P. Upper mantle structure: global isotropic and anisotropic elastic tomography. *Treat. Geophys.* **1**, (in the press).
- Gung, Y., Panning, M. & Romanowicz, B. Global anisotropy and the thickness of continents. *Nature* **422**, 707–711 (2003).
- Marone, F., Gung, Y. & Romanowicz, B. 3D radial anisotropic structure of the North American upper mantle from inversion of surface waveform data. *Geophys. J. Int.* (submitted).
- Gripp, A. E. & Gordon, R. G. Young tracks of hotspots and current plate velocities. *Geophys. J. Int.* **150**, 321–361 (2002).
- Smith, D. B., Ritzwoller, M. H. & Shapiro, N. M. Stratification of anisotropy in the Pacific upper mantle. *J. Geophys. Res.* **109**, B11309, doi:10.1029/2004JB003200 (2004).
- Tanimoto, T. & Anderson, D. L. Lateral heterogeneity and azimuthal anisotropy of the upper mantle: Love and Rayleigh waves 100–250 s. *J. Geophys. Res.* **90**, 1842–1858 (1985).
- Montagner, J.-P. & Tanimoto, T. Global upper mantle tomography of seismic velocities and anisotropies. *J. Geophys. Res.* **96**, 20337–20351 (1991).
- Simons, F., Van der Hilst, R., Montagner, J.-P. & Zielhuis, A. Multimode Rayleigh wave inversion for heterogeneity and azimuthal anisotropy of the Australian upper mantle. *Geophys. J. Int.* **151**, 738–754 (2002).
- Fouch, M. J., Fischer, K. M., Parmentier, E. M., Wyssession, M. E. & Clarke, T. J. Shear wave splitting, continental keels, and pattern of mantle flow. *J. Geophys. Res.* **105**, 6255–6275 (2000).
- Rondenay, S., Bostock, M. G., Hearn, T. M., White, D. J. & Ellis, R. M. Lithospheric assembly and modification of the SE Canadian Shield: Abitibi-Grenville teleseismic experiment. *J. Geophys. Res.* **105**, 13735–13754 (2000).
- Eaton, D., Frederiksen, A. & Miong, S.-K. Shear-wave splitting observations in the lower Great Lakes region: Evidence for regional anisotropic domains and keel-modified asthenospheric flow. *Geophys. J. Lett.* **31**, L07610, doi:10.1029/2004GL019438 (2004).
- Babuška, V., Montagner, J.-P., Plomerová, J. & Girardin, N. Age-dependent large-scale fabric of the mantle lithosphere as derived from surface-wave velocity anisotropy. *Pure Appl. Geophys.* **151**, 257–280 (1998).
- Kay, I. et al. Shear wave splitting observations in the Archean Craton of Western Superior. *Geophys. Res. Lett.* **26**, 2669–2672 (1999).
- Levin, V., Menke, W. & Park, J. No regional anisotropic domains in the northeastern U.S. Appalachians. *J. Geophys. Res.* **105**, 19029–19042 (2000).
- Bokelmann, G. H. R. & Silver, P. G. Mantle variation within the Canadian Shield: travel times from the portable broadband Archean-Proterozoic transect 1989. *J. Geophys. Res.* **105**, 579–605 (2000).
- Currie, C. A., Cassidy, J. F., Hyndman, R. D. & Bostock, M. G. Shear wave anisotropy beneath the Cascadia subduction zone and western North American craton. *Geophys. J. Int.* **157**, 341–353 (2004).
- Gaherty, J. B. A surface wave analysis of seismic anisotropy beneath eastern North America. *Geophys. J. Int.* **158**, 1053–1066 (2004).
- Li, X.-D. & Romanowicz, B. Comparison of global waveform inversions with and without considering cross branch coupling. *Geophys. J. Int.* **121**, 695–709 (1995).

Supplementary Information is linked to the online version of the paper at www.nature.com/nature.

Acknowledgements We thank IRIS-DMC, the Geological Survey of Canada and the Northern California Earthquake Data Center for distributing the data used in this study. This work was partially supported through an NSF grant and a grant from the Stefano Franscini Foundation (Switzerland).

Author Information Reprints and permissions information is available at www.nature.com/reprints. The authors declare no competing financial interests. Correspondence and requests for materials should be addressed to B.R. (barbara@seismo.berkeley.edu).

METHODS

Anisotropic parametrization. In a medium characterized by weak general anisotropy, the local frequency shift for a multiplet pair kk' can be described as^{26–28}:

$$\begin{aligned} \delta(\omega_{kk'}(\theta, \phi)^2) = & \int_0^a A_{kk'}^0(\theta, \phi, r) \\ & + A_{kk'}^1(\theta, \phi, r)\cos(2\psi) + A_{kk'}^2(\theta, \phi, r)\sin(2\psi) \\ & + A_{kk'}^3(\theta, \phi, r)\cos(4\psi) + A_{kk'}^4(\theta, \phi, r)\sin(4\psi) dr \end{aligned} \quad (1)$$

where a is the Earth radius, θ , ϕ and r describe the position in the Earth's interior and ψ is the local azimuth. The coefficients A^0 – A^4 are functions of the elements of the elastic tensor²⁹. A^0 depends only on density and the Love parameters (A , C , F , L , N)³⁰ and is required to describe the isotropic and radial anisotropic structure. A^1 and A^2 are linear functions of $B_{c,s}$, $G_{c,s}$ and $H_{c,s}$ as defined in ref. 29, while A^3 and A^4 depend on $E_{c,s}$. The coefficients A^1 – A^4 describe the effects of azimuthal anisotropy. To reduce the number of parameters in the inversion and keep only those that are best resolved by our data set (L , N and $G_{c,s}$), we assume empirical scaling relations for the remaining Love parameters as inferred from laboratory experiments³¹. We do not consider $B_{c,s}$, $H_{c,s}$ and $E_{c,s}$ because of non-existent robust linear scaling relations and the insufficient sensitivity of our data set to these parameters. Rather than inverting for L , N and $G_{c,s}$, we equivalently parametrize our model in terms of isotropic S-velocity $v_s = \sqrt{(2L+N)/(3\rho)}$, the anisotropic parameter $\xi = N/L$ and $G_{c,s}$.

Addition of constraints from SKS splitting measurements. Assuming the simplest case of weak anisotropy with a horizontal fast symmetry axis, we express station-averaged SKS splitting measurements (apparent delay time δt and fast-axis direction Ψ) as a function of elastic parameters as⁵:

$$\delta t \sin 2\Psi = \int_0^a \frac{1}{v_s^0(z)L^0(z)} G_s(\theta, \phi, z) dz \quad (2)$$

$$\delta t \cos 2\Psi = \int_0^a \frac{1}{v_s^0(z)L^0(z)} G_c(\theta, \phi, z) dz \quad (3)$$

where the superscript 0 refers to the parameters of the one-dimensional reference model. In the original derivation⁵ the quantity L rather than L_0 is used in the denominator. With the assumption of weak anisotropy, these expressions are equivalent.

Equations (2) and (3) do not imply any assumptions on the number of anisotropic layers, but they are valid for a horizontally stratified medium with an arbitrary number of plane layers. These formulas are completely equivalent to those for the case of several anisotropic layers derived in other studies^{32–34}.

Equations (2) and (3) have been derived using approximations valid only at periods longer than 10 s. Broad-band SKS waves have their peak energy around 10–15 s and the splitting parameters used in this study (Supplementary Table 1) have been measured at frequencies within the range of validity of the approximation underlying these expressions, so the use of equations (2) and (3) in this context is justified.

For each single station with azimuthally averaged SKS splitting measurements (Supplementary Table 1), two equations, equally weighted, are added to the inverse problem, where the data are combinations of δt and Ψ into $\delta t \sin 2\Psi$ and $\delta t \cos 2\Psi$, as per equations (2) and (3).

Conversely, to calculate δt and Ψ predicted by a given depth-dependent anisotropic model, the expressions above can also, equivalently, be rewritten to:

$$\delta t = \left(\left(\int_0^a \frac{1}{v_s^0(z)L^0(z)} G_s(\theta, \phi, z) dz \right)^2 + \left(\int_0^a \frac{1}{v_s^0(z)L^0(z)} G_c(\theta, \phi, z) dz \right)^2 \right)^{1/2} \quad (4)$$

$$\tan 2\Psi = \frac{\int_0^a \frac{1}{v_s^0(z)L^0(z)} G_s(\theta, \phi, z) dz}{\int_0^a \frac{1}{v_s^0(z)L^0(z)} G_c(\theta, \phi, z) dz} \quad (5)$$

Inversion. We first correct our waveform data for structure outside the region of study using the global radially anisotropic model SAW642AN (ref. 35). This model has no azimuthal anisotropy outside the target region. Because azimuthal anisotropy inside the study region is constrained by a good azimuthal coverage (Supplementary Fig. 6), the effect of not correcting the waveforms for the three-dimensional azimuthal anisotropy structure outside the target region should

have a minimal effect on the obtained model. We apply crustal corrections computed using CRUST5.1 (ref. 36) for vertical and longitudinal component data and the crustal portion of SAW24B16 (ref. 37) for transverse component data. We solve the inversion problem iteratively using a least-squares approach³⁸.

The addition of azimuthal anisotropy to the radial anisotropic problem¹⁰ strongly increases the number of unknowns. Stronger regularization needs to be applied, where the choice of the damping parameters is rather subjective. For instance, the radial and azimuthal anisotropic structures are known to be affected by strong tradeoffs, in which by tuning individual damping parameters one can force the required anomalies to favour one or the other portion of the model space. In addition, the amplitude of anisotropy strongly depends upon regularization in the inverse problem. To minimize the subjectivity of the choices required, we opted for an iterative solution in two steps.

In the first step, we consider only radial anisotropy and simultaneously invert for v_s and ξ , while keeping the azimuthal anisotropic portion of the model fixed (that is, initially the azimuthal anisotropy terms are zero). The radial anisotropic part of the problem is well understood, thanks to a variety of tests on resolution and tradeoffs¹⁰. In a second step, we keep the obtained radial anisotropic model fixed and vary only the model parameters related to azimuthal anisotropy. In this case we need to adjust only one damping parameter, mainly controlling the amplitude of azimuthal anisotropy. Because only relatively small improvements in variance reduction are afforded by decreasing damping, we guided our choice on the basis of the theoretical expected amplitude of anomalies. However, the recovered fast-axis direction is a robust feature, which is not influenced by the choice of the damping parameter. The anisotropy strength is, in contrast, poorly constrained, in particular at depths exceeding 200 km, and usually strongly underestimated (>50%) (Supplementary Figs 2–4). The radial anisotropic model can subsequently be updated keeping the azimuthal portion of the model space fixed, although we have verified that adjustments due to the introduction of azimuthal anisotropy are minor.

The model is parametrized laterally in level 4 spherical splines³⁹ (equivalent to a spherical harmonics expansion of about degree 24) and vertically in cubic splines.

Goodness of the fit. We quantitatively assess the goodness of the fit of our model to the surface-wave and SKS splitting data sets using the variance reduction computed according to the following expressions.

For surface waves:

$$\sigma_{\text{surfacewave}}^2 = 1 - \frac{\sum_{i=1}^{N_{\text{sw}}} (d_i - s_i)^2}{\sum_{i=1}^{N_{\text{sw}}} d_i^2} \quad (6)$$

where d and s are the observed and synthetic surface-waveform data, the index i refers to a particular point of the time-domain surface waveform considered, and the summation is over all the waveform data points in the data set.

For SKS splitting measurements:

$$\sigma_{\text{SKS}}^2 = 1 - \frac{\sum_{i=1}^{N_{\text{SKS}}} \left[\left((\delta t \sin 2\Psi_i)_{\text{observed}} - (\delta t \sin 2\Psi_i)_{\text{synthetic}} \right)^2 + \left((\delta t \cos 2\Psi_i)_{\text{observed}} - (\delta t \cos 2\Psi_i)_{\text{synthetic}} \right)^2 \right]}{\sum_{i=1}^{N_{\text{SKS}}} \left[(\delta t \sin 2\Psi_i)_{\text{observed}}^2 + (\delta t \cos 2\Psi_i)_{\text{observed}}^2 \right]} \quad (7)$$

where δt and Ψ are station-averaged SKS splitting parameters (delay time and fast-axis direction, respectively). The datum used in the inversion to describe SKS splitting information is a combination of δt and Ψ (see above), so we use the same datum to compute the variance reduction for these measurements.

- Smith, M. L. & Dahlen, F. A. The azimuthal dependence of Love and Rayleigh waves propagation in a slightly anisotropic medium. *J. Geophys. Res.* **78**, 3321–3333 (1973); correction **80**, 1923 (1975).
- Romanowicz, B. & Snieder, R. A new formalism for the effect of lateral heterogeneity on normal modes and surface waves, II. General anisotropic perturbations. *Geophys. J. R. Astron. Soc.* **93**, 91–99 (1988).
- Larsen, E. W. F., Tromp, J. & Ekström, G. Effects of slight anisotropy on surface waves. *Geophys. J. Int.* **132**, 654–666 (1998).
- Montagner, J.-P. & Nataf, H.-C. A simple method for inverting the azimuthal anisotropy of surface waves. *J. Geophys. Res.* **91**, 511–520 (1986).
- Love, A. E. H. *A Treatise on the Mathematical Theory of Elasticity* (Cambridge Univ. Press, Cambridge, 1927).
- Montagner, J.-P. & Anderson, D. L. Petrological constraints on seismic anisotropy. *Phys. Earth Planet. Inter.* **54**, 82–105 (1989).
- Silver, P. G. & Savage, M. K. The interpretation of shear-wave splitting parameters in the presence of two anisotropic layers. *Geophys. J. Int.* **119**, 949–963 (1994).
- Wolfe, J. W. & Silver, P. G. Seismic anisotropy of oceanic upper mantle: Shear wave splitting methodologies and observations. *J. Geophys. Res.* **103**, 749–771 (1998).
- Rümpker, G. & Silver, P. G. Apparent shear-wave splitting parameters in the presence of vertically varying anisotropy. *Geophys. J. Int.* **135**, 790–800 (1998).
- Panning, M. P. & Romanowicz, B. A three dimensional radially anisotropic model of shear velocity in the whole mantle. *Geophys. J. Int.* **167**, 361–379 (2006).

36. Mooney, W. D., Laske, G. & Masters, T. G. CRUST5.1: a global crustal model at 5°x 5°. *J. Geophys. Res.* **103**, 727–747 (1998).
37. Mégnin, C. & Romanowicz, B. The 3D shear velocity structure of the mantle from the inversion of body, surface and higher mode waveforms. *Geophys. J. Int.* **143**, 709–728 (2000).
38. Tarantola, A. & Valette, B. Generalized nonlinear inverse problems solved using the least squares criterion. *Rev. Geophys. Space Phys.* **20**, 219–232 (1982).
39. Wang, Z. & Dahlen, F. A. Spherical-spline parameterization of three-dimensional Earth models. *Geophys. Res. Lett.* **22**, 3099–3102 (1995).